Advancements in Planetary Unstructured Equivalent Source Inversion and Current Circulation Modeling Technology for Earth's Magnetic Field

Boxin Zuo[1], Lizhe Wang[1] , Xiangyun Hu[2],Yi Cai[1] , Mason Andrew Kass[3]

[1] China University of Geosciences, School of Computer Sciences, Wuhan 430078, China.

[2] China University of Geosciences, Institute of Geophysics and Geomatics, Wuhan 430074, China.

[3]Aarhus University, Department of Geoscience, Denmark.

Corresponding author

Boxin Zuo: boxzuo@cug.edu.cn, ORCID 0000-0002-7274-1081

Tel: +86-13657263837

Address: No.388 Lumo Road, Wuhan, China

Key Points:

- Introduction of a Novel Technology for Constructing Planetary Equivalent Magnetization Sources of Geomagnetic Field.
- Inversion of 3-D Unstructured Tetrahedral Equivalent Sources in Cartesian Coordinates for Geomagnetic Modeling.
- Enhancing Geomagnetic Field Analysis through 3-D Electric Current Circulation Modeling with an Equivalent Source.

Abstract

This study presents a novel approach to modeling the Earth's geomagnetic field, which originates from electric currents approximately 2,900 km beneath the surface, crucial for understanding planetary dynamics. We introduce a method for inverting a planetary-scale equivalent magnetization source and develop a 3-D equivalent electric current circulation model from this source, enhancing understanding of these deep currents. This research signifies the first use of unstructured tetrahedral magnetization inversion technology for planet-scale magnetic data interpretation and equivalent source model construction. Validated through a synthetic case study, the method is applied to the International Geomagnetic Reference Field (IGRF) and SWARM satellite datasets, comprising 35,768 magnetic vectors from two orbital altitudes. Employing various mesh configurations, we construct and compare detailed current source models from these datasets. The effectiveness of our equivalent current sources is confirmed by comparison with dynamo research findings, demonstrating significant advancements in geomagnetic field modeling, particularly in interpretability, and providing novel insights into Earth's magnetic phenomena.

Plain Language Summary

The Earth's geomagnetic field plays a crucial role in shielding us from harmful solar winds and cosmic rays. This protective field arises from electric currents generated within the Earth's core, a dynamic realm composed of circulating liquid iron and nickel around a solid inner core. Measuring these deep-seated currents directly poses a significant challenge due to their inaccessibility. To date, scientists have effectively modeled the Earth's magnetic field using advanced techniques like spherical harmonic analysis and the concept of magnetic dipoles.

However, a major hurdle remains in accurately depicting the geomagnetic field using magnetization volumes of arbitrary shapes and in unraveling the intricate patterns of the core's current circulation. In this study, we unveil a novel method that enables the creation of a detailed, three-dimensional model of the geomagnetic field's equivalent magnetization source comprising millions of unstructured tetrahedrons, provides a deeper and more nuanced insight into the Earth's inner workings. Our comprehensive 3-D model closely aligns with the currents' circulation patterns observed in dynamo research, affirming the validity and effectiveness of our approach. This pioneering method marks a significant leap forward in our understanding of the geomagnetic field, offering an invaluable tool for future research in Earth sciences.

1. Introduction

The Earth's magnetic field is generated by electric currents flowing deep within the core, approximately 2,900 km beneath the surface. Directly measuring these internal currents presents formidable challenges due to the inaccessible and heterogeneous nature of the deep core media. The geomagnetic field's secular variations, exemplified by phenomena such as the South Atlantic Anomaly (SAA), asymmetry in the main dipolar field, intense equatorial gyres at the core-mantle boundary (CMB) (Jackson 2003), and significant static flux bundles observed in Canada and Siberia (Bloxham & Gubbins 1985), are all attributed to these fluid electric currents (Davies & Constable 2017). Consequently, modeling the geomagnetic field to explore these internal electric current sources has been a significant and extensively researched task over recent decades.

Spherical harmonic analysis (SHA) has been historically the primary method for describing the geomagnetic field (Whaler & Gubbins, 1981; Alken et al., 2021). To gain a deeper understanding of the geomagnetic field's source and to predict short-term secular variations, researchers have introduced equivalent source methods, such as the magnetic dipole approach (Dampney, 1969; Hansen & Miyazaki, 1984). Bhattacharyya and Chan (1977) suggested the use of a set of magnetic dipoles placed on a surface as the equivalent source for interpolating magnetic data across various surfaces. Initially introduced by Mayhew (1979) for crustal geomagnetic field modeling, the Equivalent Source Dipole (ESD) method has since been widely applied in diverse planetary magnetic field studies. For instance, Purucker et al. (2000) used the ESD method to invert the radial magnetic field of Mars. Langlais et al. (2004) enhanced the ESD technique to model the Martian lithospheric magnetic field's three components. Oliveira et al. (2015) developed a time-dependent equivalent source dipole model for planetary magnetic fields and their secular variations. Buffett (2015) investigated geomagnetic polarity transitions using an

ESD model, and Langlais et al. (2019) introduced a new ESD model of the Martian crustal magnetic field using data from the MGS and MAVEN satellites. Most recently, Hood et al. (2021) employed the ESD technique to produce a comprehensive map of the lunar crustal magnetic field. These studies collectively demonstrate that the dipole source equivalent is a potent and efficient approach for addressing the complexities of the geomagnetic field and achieving well-fitting data.

Additional efforts have been directed towards improving source information in geomagnetic field models by using current loops as more realistic equivalent sources for aligning with observations of the geomagnetic field (Zidarov & Petrova, 1974). Peddie (1979) created eleven sets of current loops based on the Biot-Savart law, designed to fit the geomagnetic field. He proposed that these loops could effectively be considered as dipoles with negligibly small radii. Expanding on this concept, Demina and Farafonova (2016) investigated the possibilities and errors involved in estimating the parameters of current loops of varying radii. Recently, Rong et al. (2021) methodically inverted parameters of single circular loops to analyze the geomagnetic dipole field. They utilized magnetic vectors sampled from Swarm satellites, providing a comprehensive discussion on the equivalence between dipole and current loop sources in geomagnetic modeling.

While dipole and equivalent current loop sources have received extensive research attention over the past decades, there has also been a growing focus on the mesh-based volume equivalent source approach in small-scale regional magnetic surveys. Hansen and Miyazaki (1984) conceptualized a planar equivalent source composed of divided structured mesh elements. Li and Oldenburg (2010) innovated further by employing a sparse representation in the wavelet domain to construct a mesh-based equivalent susceptibilities source. Their work demonstrated

that this approach enhances the stability of data modeling in low-latitude regions. Pilkington and Boulanger (2017) conducted a comparative analysis between source-based and field-based methods, highlighting the potential of equivalent source methods for high-accuracy regional magnetic field modeling. In an effort to minimize data prediction misfits, Li et al. (2019) expanded the mesh-based source layer from a single to a double layer. More recently, Zuo et al. (2020) showed that the accuracy of geomagnetic field continuation and transformation could be further improved by approximating the actual source with a 3-D deep mesh and depth-weighted functions, thereby enhancing the resemblance of the inverted model to the actual source.

While numerous methods employing volume equivalent sources exist, their application in the study of planetary magnetic fields remains unexplored. A primary challenge arises from the fact that these methods are predominantly tailored to model secondary fields, which are induced by Earth's geomagnetic field. In contrast, planetary geomagnetic fields, originating from internal dynamo processes, or remanent magnetization, exhibit fundamentally different mechanics. Additionally, fitting observational data within spherical or Cartesian coordinates using an equivalent source proves more arduous for planetary fields than for regional magnetic field modeling in structured meshes. Recent advancements demonstrate the efficacy of utilizing a 3D unstructured grid for magnetic data inversion (Zuo et al., 2021). The approach shows significant potential in accurately recovering sources with complex geometries and enhancing data fitting precision. Building upon previous research in magnetization dipole equivalent sources and volume equivalent source studies, we propose the development of a 3-D unstructured magnetization equivalent source. This approach would involve employing a magnetization forward modeling method within Cartesian coordinates, in conjunction with the development of an equivalent current sources model, which aimed at enhancing the understanding of the

geomagnetic field. The potential and practical applicability of this method are corroborated through both synthetic and real data examples, drawing upon insights from previous dynamo studies.

2.1 Forward Modeling of Unstructured Magnetization Sources

Consider a static magnetic field generated by an unstructured magnetization vector model $\mathbf{m} = \left[\mathbf{m}_x, \mathbf{m}_y, \mathbf{m}_z\right]$, under the assumption of no free currents. In accordance with Maxwell's equations, this magnetic field $\mathbf{B}$ can be described by the Poisson equation, represented as Eq. (1):

$$-\nabla \cdot \left(\mu_0(\nabla\phi - \mathbf{m})\right) = 0 \quad \text{in } \Omega \in \Re^3 \tag{1a}$$

$$\mathbf{B} = \mu_0 \nabla\phi \tag{1b}$$

In this context, ϕ represents the potential field within the 3-D modeling domain Ω, as defined in Eq. (1a), and μ_0 is the permeability of free space. We utilized the third boundary condition, which describes the behavior of ϕ and its derivatives $\partial\phi/\partial\mathbf{n}$ at a specific distance r and direction $\hat{\mathbf{r}}$ from the source $\mathbf{m}$ to the modeling boundary, as expressed in Eq. (2).

$$\frac{\partial\phi}{\partial\mathbf{n}} + \left(\frac{\hat{\mathbf{r}}\cdot\hat{\mathbf{n}}}{r}\right)\phi = 0 \qquad \text{on } \Gamma_s \tag{2}$$

Here, $\hat{\mathbf{n}}$ represents the outward normal vector of the boundary Γ_s. Subsequently, a weak form of the governing equations is derived using Galerkin's method, as outlined in Eq. (3):

$$R = \int_{\Omega} \phi \nabla w d\Omega + \int_{\Omega} w \nabla \cdot \mathrm{M} d\Omega - \int_{\Gamma_s} w \frac{\partial\phi}{\partial\mathbf{n}} d\Gamma_s \tag{3}$$

In this framework, w denotes the basis function. We have developed a classical quadratic

finite element discretization scheme, as described by Jin (2002), within Cartesian coordinates. This scheme is employed to solve for the unknown potential field ϕ, details of which are elaborated in Text S1 and illustrated in Fig. S1. Subsequently, the magnetic field is estimated according to $\mathbf{B} = \mu_0 \nabla \phi$.

2.2 Equivalent Magnetization Model Inversion

An unstructured mesh Finite Element (FE) inversion scheme has been designed, building upon the forward modeling method. Taking into account the planetary spherical inverse model within Cartesian coordinates, we incorporate both the depth-weighted function and the regularization term into the inverse objective function. This is succinctly presented in Eq. (4).

$$\begin{aligned} &\text{minimze} \quad \phi = \phi_d + \phi_m = \frac{1}{2}\left\|\mathbf{W}_d\left(\mathrm{F}(\mathbf{m}) - \mathbf{d}^{obs}\right)\right\|^2 + \frac{\beta}{2}\left\|\mathbf{W}_s\mathbf{W}_r(\mathbf{m}-\mathbf{m}_0)\right\|^2 \\ &\text{where} \quad \mathbf{W}_r^{\,2} = \frac{1}{(R+h)^3} \end{aligned} \tag{4}$$

$\mathbf{m}$ represents the magnetization vector, which is derived by inverting the observational data, $\mathbf{d}^{obs} = \left[\mathrm{B}_x, \mathrm{B}_y, \mathrm{B}_z\right]$. The term $\mathbf{W}_d$ corresponds to the measurement bias of the data. The variable R denotes the radial distance from the discretized element to the sphere's surface, while hh signifies the altitude of the observation. $\mathbf{m}_0$ is the reference model vector. The spatially dependent weighting function, denoted as $\mathbf{W}_r^{\,2}$, is calculated based on the volume of each tetrahedron element in the mesh. $\mathbf{W}_s$ is the smoothing matrix. The regularization coefficient, β, can be estimated by balancing the data misfit error and the model dispersion. To solve the objective function iteratively, a nonlinear conjugate gradient optimization method, commonly applied in electromagnetic field inverse problems, is employed (referencing Newman & Alumbaugh 2000). Furthermore, we have derived the gradient function of this objective function,

as shown in Eq. (5)

$$\frac{\partial \Phi}{\partial \mathbf{m}} = \mathbf{J}_s^T \mathbf{W}_d{}^T \mathbf{W}_d \left(F(\mathbf{m}) - \mathbf{d}^{obs} \right) + \beta \mathbf{W}_s{}^T \mathbf{W}_s \mathbf{W}_r{}^T \mathbf{W}_r \left(\mathbf{m} - \mathbf{m}_0 \right) \tag{5}$$

where $\mathbf{J}_s$ is the sensitive matrix, as Eq. (6) expressed.

$$\mathbf{J}_s = \begin{bmatrix} \partial \mathbf{B}_x / \partial \mathbf{m} \\ \partial \mathbf{B}_y / \partial \mathbf{m} \\ \partial \mathbf{B}_z / \partial \mathbf{m} \end{bmatrix} = \mu_0 \begin{bmatrix} Q_x \\ Q_y \\ Q_z \end{bmatrix} \frac{\partial \phi}{\partial \mathbf{m}} \tag{6}$$

2.2 Estimation of the Equivalent Current Circulation Mode

The toroidal currents $\mathbf{J}_T$ within the Earth's core are integral in generating the observed geomagnetic field $\mathbf{B}$. In this study, we propose a methodology to estimate an equivalent current circulation model $\mathbf{J}_\mathbf{m}$ based on the inverted equivalent 3-D magnetization model $\mathbf{m}$ derived from $\mathbf{B}$, as delineated in Eq. (7).

$$\mathbf{J}_\mathbf{m} = \nabla \times \mathbf{m} \tag{7}$$

It is a typical unique solving problem that can directly transform a magnetization model $\mathbf{m}$ to a corresponding current model $\mathbf{J}_\mathbf{m}$. In accordance with classical electromagnetic theory, this processes adhere to Ampère's law (Text S3). This electric current model constructing scheme avoid using the inaccessibility of physical properties for the deep, inhomogeneous core media. As for solving the magnetization model is a non-unique problem, the derived current model $\mathbf{J}_\mathbf{m}$ is also a non-unique equivalent magnetization electric current. We transfer the non-real existing magnetization vectors $\mathbf{m}$ to an equivalent current circulation model, which is an approximated solution for conjecturing the actual electric currents in the deep core interior to facilitate and

enhance the understanding of the origination geomagnetic field.

Transforming a magnetization model $\mathbf{m}$ into a corresponding current model $\mathbf{J}_m$ represents a typical unique solution problem, aligning with classical electromagnetic theory and adhering to Ampère's law, as detailed in Text S3. This method of constructing an electric current model circumvents the challenges posed by the inaccessibility of physical properties in the deep, inhomogeneous core. Given the non-uniqueness of the magnetization model solution, the resultant current model $\mathbf{J}_m$ also embodies a non-unique equivalent of the magnetization electric current. We convert the non-realistically existing magnetization vectors $\mathbf{m}$ into an equivalent current circulation model. This approach serves as an approximated solution, offering insights into the actual electric currents deep within the core and thereby facilitating a better understanding of the geomagnetic field's origin.

3. Results

3.1 Synthetic Example

To validate our inverse scheme, we use a synthetic model that consists of a high-conductivity circular ring. This ring has an outer diameter of 2,000 kilometers and a width of 100 kilometers, and it carries a current with an intensity of 10 A/m², as depicted in Fig. 1a., designed to simulate an equatorial toroidal current beneath the core-mantle boundary (CMB) within the Earth's core. Employing Eq. (7), we derive the equivalent magnetization model $\mathbf{m}$ for this current. As illustrated in Fig. 1a, the distribution of the equivalent magnetization vector model is notably non-uniform (see subplot in Fig. 1a), with the highest magnetization vector magnitudes (1.1E6 A/m) concentrated near the circular surface, decreasing rapidly towards the ring's center. This magnetization model $\mathbf{m}$ effectively replicates a magnetic field $\mathbf{B}$ with an overall dipole-

field characteristic, as shown in Fig. 1b. For our synthetic case, we use 35,768 magnetic observation vector data points, evenly distributed at altitudes of 450 km and 530 km, to simulate measurements from a dual-satellite orbit scenario. To enhance visual clarity, only half sections of these observation points are shown in Fig. 1a. The inversion mesh in our study comprises 2,337,505 unstructured tetrahedrons (illustrated in Fig. S1), ensuring a finely divided and uniform mesh for the core space."

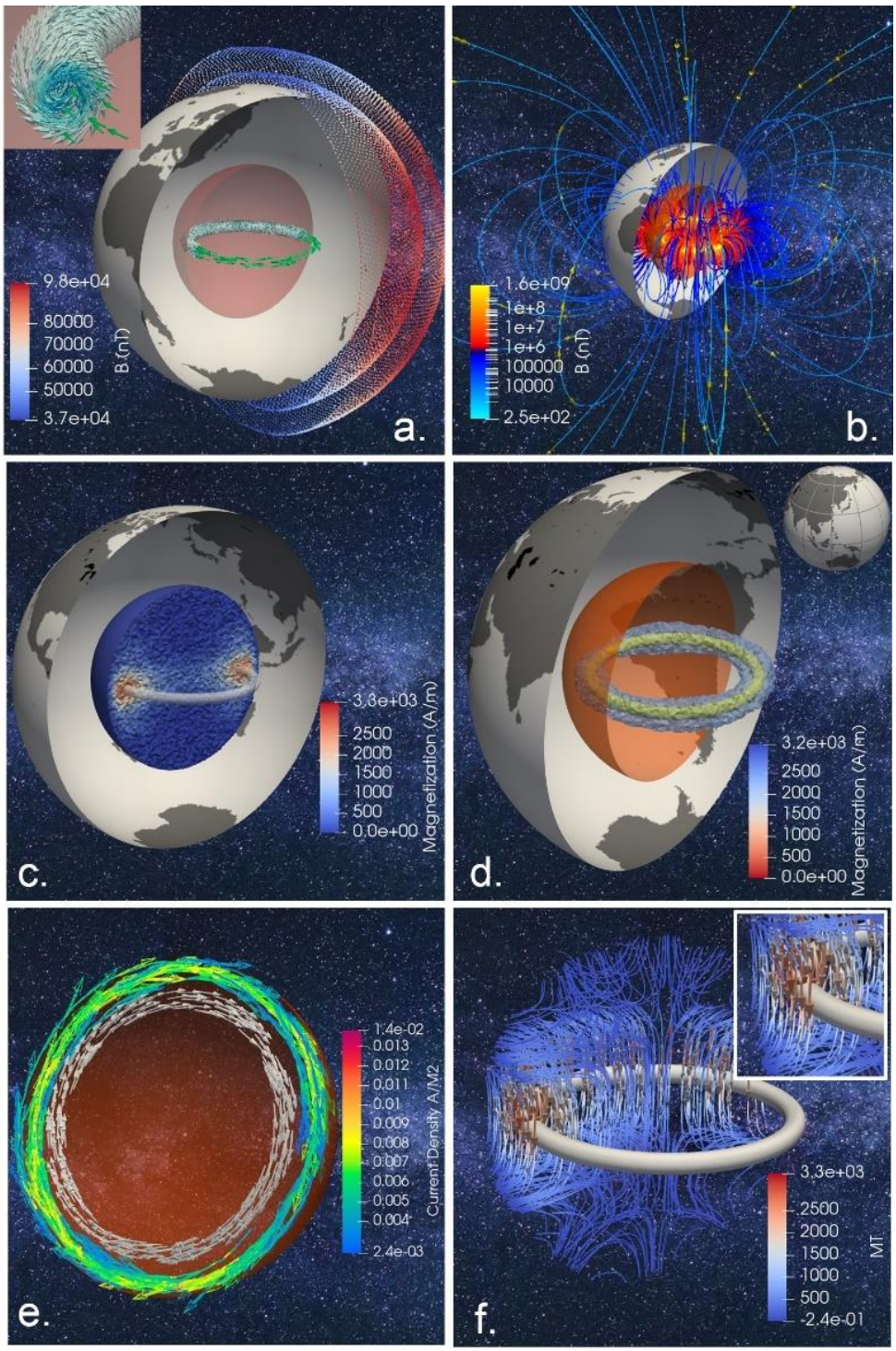

Figure 1: Synthetic Forward and Inversion Example

a. Simulated Circular Current (indicated by green arrows) within the core region (represented by a red sphere section) alongside the equivalent magnetization model (depicted with light blue

arrows) in the subplot. Observation sphere's surface at altitudes of 480 km and 530 km is shown, with the outer section radius exaggerated for clarity. b. Simulated Magnetic Field visualized in 3-D space. c. Section of the Inverted Magnetization Model, with the actual magnetization model denoted by a gray circle. d. Recovered Magnetization Model, highlighting areas where values exceed 2,000 A/m (gray circle). e. Comparative analysis of the recovered and actual current in the core's Southern hemisphere. f. Detailed section of Recovered Magnetization Vectors, with an enlarged detail in the subplot.

In our inversion process, we achieved a well-converged misfit of 0.68%, leading to the successful recovery of a 3D magnetization model, as depicted in Figs. 1c and 1d. From this magnetization model, we derived a current circulation model, which is presented in Fig. 1e. The magnetic field generated by the circular current displays a distinct downward dipole-like field characteristic (Fig. 1b), closely resembling the dipole component of the Earth's magnetic field in terms of strength and 3D orientation.

The inverted equivalent magnetization source $\mathbf{m}$ is positioned at depths that correspond accurately with the actual model, as illustrated in Figures 1c and 1d. Its maximum magnitude reaches 3,171 A/m, noticeably smaller than that of the actual model. This discrepancy partly arises because the volume of the recovered model $\mathbf{m}$ is larger than that of the actual one. Notably, the estimated current, positioned at a depth of 3,179 km, is shallower by 600 km compared to the actual currents at 3,779 km depth, as illustrated in Fig. 1e. To understand the origin of this bias, we examined a cross-section of the inverted magnetization vectors (Fig. 1f). A comparison of the recovered magnetization vectors near the source region (subplot in Fig. 1f) with the actual magnetization source vectors (subplot in Fig. 1a) reveals significant differences in their orientations. The directions of the inverted magnetization vectors align with the primary

dipole field direction (downwards in the source region). This is consistent with classical inverse procedures, where only magnetization sources that conform to the observed field direction can be recovered. For example, the anomalous field generated by locally opposing magnetization vectors (upwards) in the rotational magnetization source (Fig. 1a, subplot) is neutralized by the intense dipole field and becomes indiscernible in the observational data, and the corresponding upwards magnetization sources also remain unrecovered. Therefore, this bias originates from the limited information contained in the observational data and cannot be rectified merely by improving the inversion method.

3.2 IGRF Example

Magnetic vector data points, totaling 35,768, gathered at altitudes of 450 km and 530 km above the Earth's surface, are sourced from the IGRF-13 dataset (Alken et al., 2021). These data points follow the configuration depicted in Text S2 and are collected with the time parameter 'frozen' at January 1, 2023. In our analysis, we also take into account the electrical conductivity of the inner core, incorporating this region into the inversion process. The inversion mesh utilized is the same as the one used in the synthetic experiment (as shown in Fig. S1). Notably, the inversion process achieves a commendable data prediction error level of 1% for the core's equivalent magnetization model $\mathbf{m}$. Subsequently, the current circulation model is determined based on this magnetization model, as illustrated in Figures 2a to 2f.

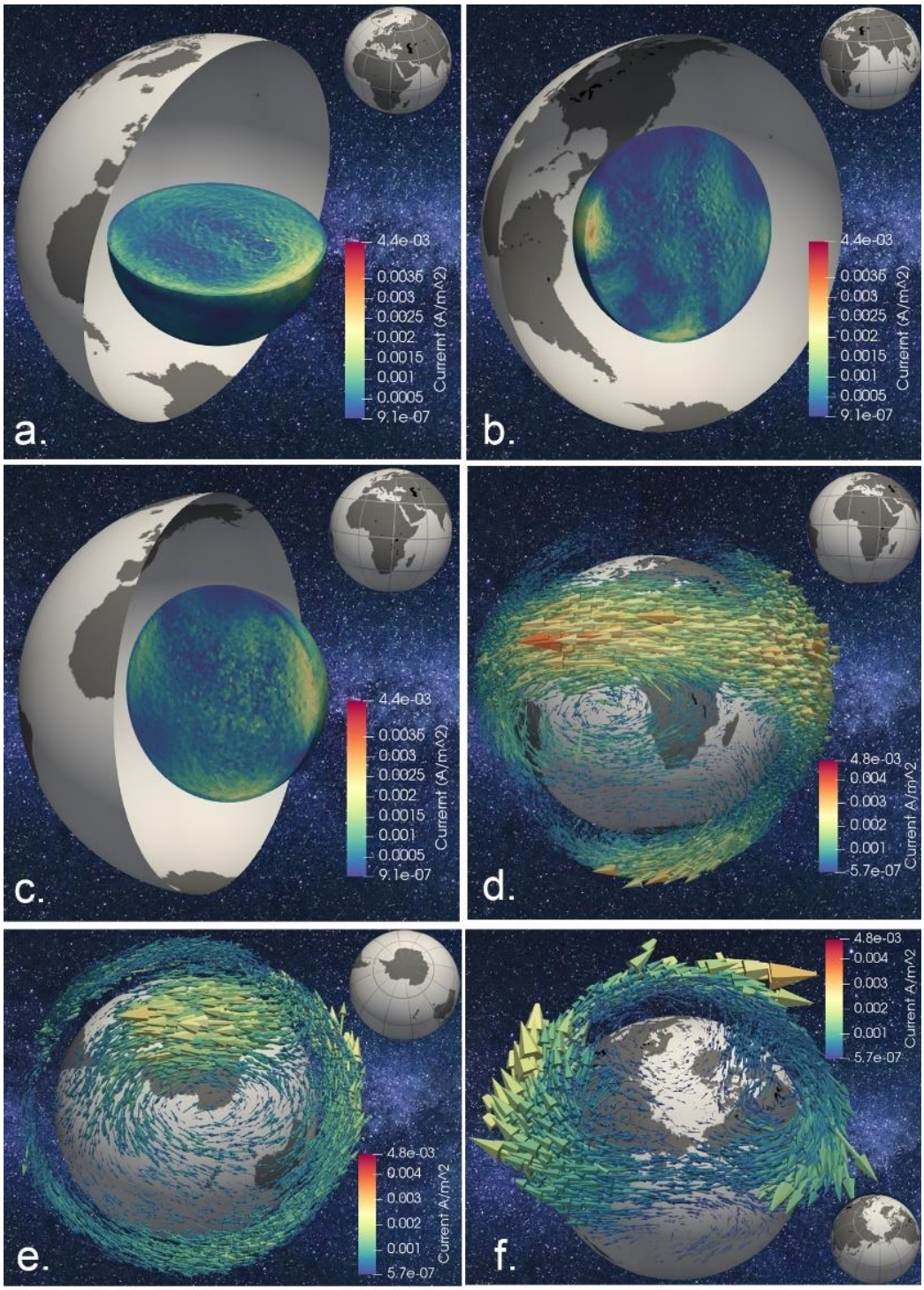

254

255 Figure 2: Inverted Electric Current Circulation Model Derived from the IGRF Dataset.

256 a. Horizontal Section of the Current Model within the Core Region. The large semi-gray sphere

257 is a visual aid representing the Earth's surface for locational context. b. Vertical Section of the

Current Model along 0° Longitude, showing the current distribution and flow at this meridian. c. Vertical Section of the Current Model along 90° Longitude, illustrating the currents along this longitudinal slice. d. Vectors Representation of the Current Model beneath the African Hemisphere within the Core. A gray sphere, positioned 800 km below the core-mantle boundary (CMB), is used to enhance the visibility of shallow intense currents. The sizes and lengths of the vectors are indicative of the corresponding current intensities. e. Vectors Representation of the Current Model beneath the Antarctic Hemisphere, depicting the current flow and intensity in this region. f. Vectors Representation of the Current Model beneath the Arctic Ocean Hemisphere.

As illustrated in the sectional view of Fig. 2a, intense currents are predominantly concentrated near the core-mantle boundary (CMB). The highest-intensity currents within the current circulation model are located in the equatorial region. Notably, beneath the South American continent, the equatorial gyre exhibits a discontinuity (indicated by red arrows) and extends into the deep core interior. Fig. 2b and 2c showcase the presence of weaker toroidal circular currents throughout the core space, which will be discussed in the following section.

Vector maps have been employed to analyze the circulation patterns of these intense currents near the CMB surface (from the CMB up to a depth of 800 km). As depicted in Fig. 2d, the most intense electric currents traverse the African hemisphere in a clockwise direction, spanning from the eastern Indian Ocean to the Pacific Ocean. A significant retrograde current branches off beneath the South Atlantic Ocean, moving eastward and forming a coherent gyre structure. This gyre then connects with a high-latitude currents gyre observed in the Antarctic region, as shown in Fig. 2e. In contrast, currents in the North Pole region, detailed in Fig. 2f, cover a broader area but with lower intensities. Three relatively weaker current gyres are identified in Siberia, Canada, and the Arctic Ocean, as indicated in Fig. 2f.

3.2 SWARM Example

We selected a total of 24,192 magnetic vector field data points from the Swarm Level 1b data product, collected via two distinct satellite orbits: Alpha, orbiting at an altitude of 475 km, and Bravo, at 502 km above the Earth's surface (Dataset S1). These data were gathered during August 22-27, 2022, specifically between local times 22:00 and 03:00, to minimize ionospheric contributions. The simultaneous inversion of two satellite vector datasets was chosen for two primary reasons. First, the varying altitudes provide rich, gradient magnetometry-like information. Second, using the same number of observation points at a single altitude would significantly increase the number of divided cells in the model. Distributing observations across two altitudes helps mitigate this issue by avoiding the introduction of unexpected divided cells.

To ensure the reliability of the data under varying magnetic conditions, we applied stringent filters: Kp < 2, |Dst| < 20 nT, and F10.7 < 103 10^22 Wm^-2Hz^-1. This filtration was crucial to maintain data quality and focus on periods with relatively stable magnetic conditions. Additionally, we restricted the data to intervals of 500 measurement points to achieve as close to a homogenous distribution as possible, as depicted in Fig. S3.

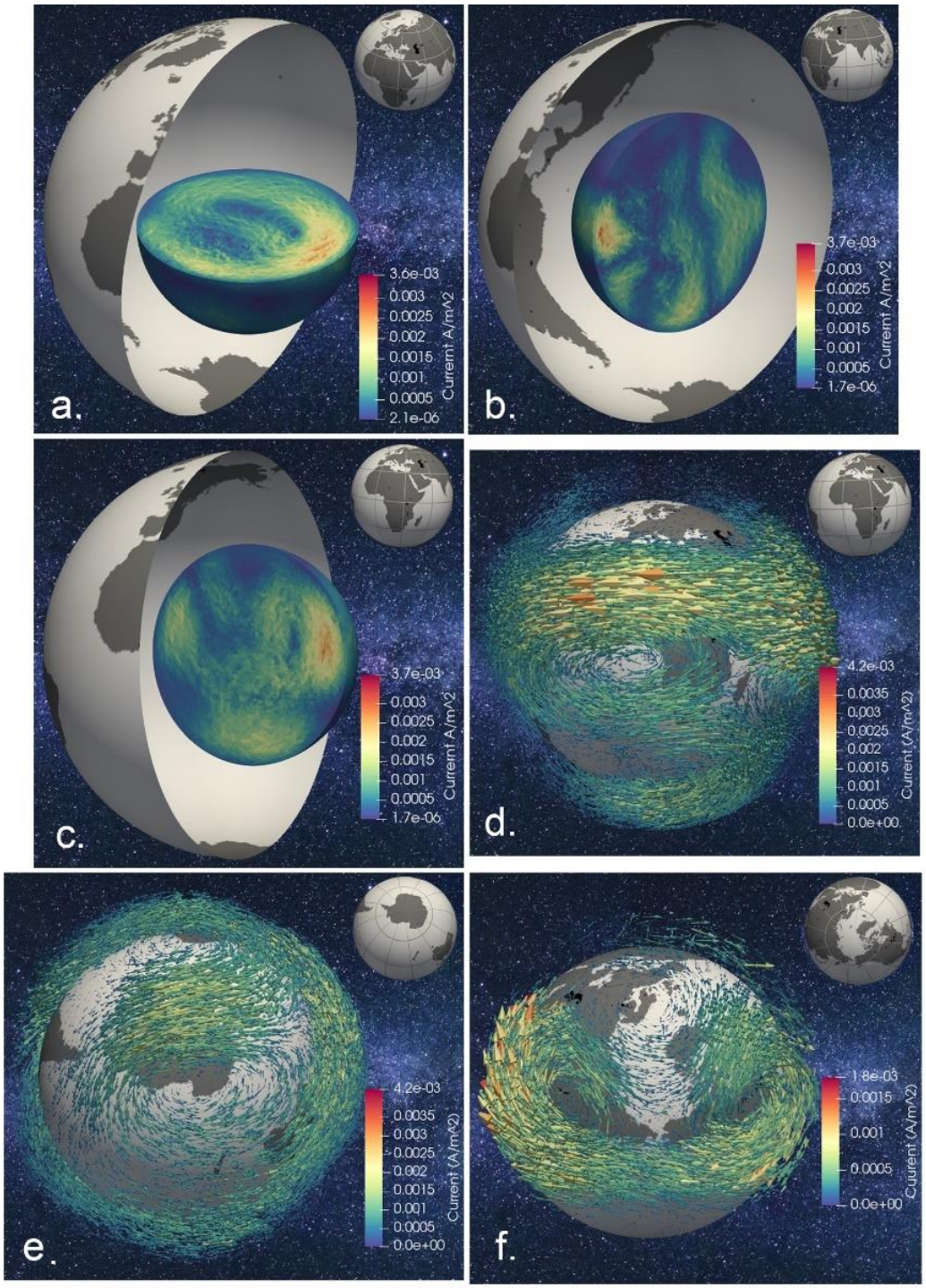

296

297 Figure 3: Inverted Electric Current Circulation Model Derived from the Swarm Dataset.

298 a. Horizontal Section of the Current Model within the Core Region, showcasing the layout and

299 flow of currents. b. Vertical Section of the Current Model along 0° Longitude, illustrating the

current distribution and dynamics at this meridian. c. Vertical Section of the Current Model along 90° Longitude. d. Vector Representation of the Current Model beneath the African Hemisphere within the Core, showing the pattern and intensity of currents. e. Vector Representation of the Current Model beneath the Antarctic Hemisphere, highlighting the current flows in this region. f. Amplified Vector Representation of the Current Model beneath the Arctic Ocean Hemisphere. The arrow lengths in each subplot are zoomed to emphasize the gyre structure, and they are not to scale across all subplots. This amplification approach is consistent across IGRF experiments

The inversion results of the Swarm dataset are illustrated using the plotting template of Fig. 2 for comparative analysis. The sections depicting inverted currents in the *x, y,* and *z* directions within the core space are presented in Figs. 3a, 3b, and 3c, respectively. Figs. 3d, 3e, and 3f provide insights into the directions and intensities of currents beneath the CMB, extending 800 km deep below the equatorial, Antarctic, and Arctic Ocean regions. An animated version of this model is available as Movie S1, and for a comprehensive overview of the full set of Swarm current examples, refer to Fig. S4.

The Swarm model still exhibits an intense toroidal current structure, as shown in Fig. 3a. Although the maximum current intensity of this Swarm section is 3.6E-3 A/m², which is less than that of the corresponding IGRF model section (4.4E-3 A/m², Fig. 2a), the distributions of the equatorial current gyre in both the Swarm and IGRF model sections (Figs. 2a and 3a) are similar. This includes the discontinuity of the equatorial gyre beneath the South American continent. Similar patterns in the inverted current circulation are also observed in the other directional sections (Figs. 3b and 3c) compared to the IGRF model (Figs. 2b and 2c). For the shallow currents beneath the CMB (0-800km), the Swarm model displays a similar equatorial intense gyre extending from the eastern Indian Ocean to the Pacific Ocean in a clockwise direction,

connecting to a retrograde current gyre beneath the South Pacific Ocean (Fig. 3d). The intense current gyre located below the Antarctic hemisphere (Fig. 3e) and the weaker current gyres observed in Siberia, Canada, and the Arctic Ocean (Fig. 3f) are consistent with those in the IGRF inverted current model (Figs. 2e and 2f), exhibiting similar locations and flow patterns.

To further illuminate the 3-D structure of the inverted current model throughout the entire depth of the Earth's core, we implemented a filtering procedure to remove all currents with magnitudes less than 5.6E-4 A/m^2. This process allowed us to create a 3D current vector map focused predominantly on the more intense current flows. Given that the current circulation patterns of the IGRF model and the Swarm model are similar, only the Swarm model is depicted for simplicity and clarity. To provide a comprehensive visualization of this complex structure, we have divided the 3-D map into two vertical section segments: the Eurasia hemisphere and the American hemisphere. These segments are displayed in both top-view and side-view perspectives, as shown in Figs. 4a-d.

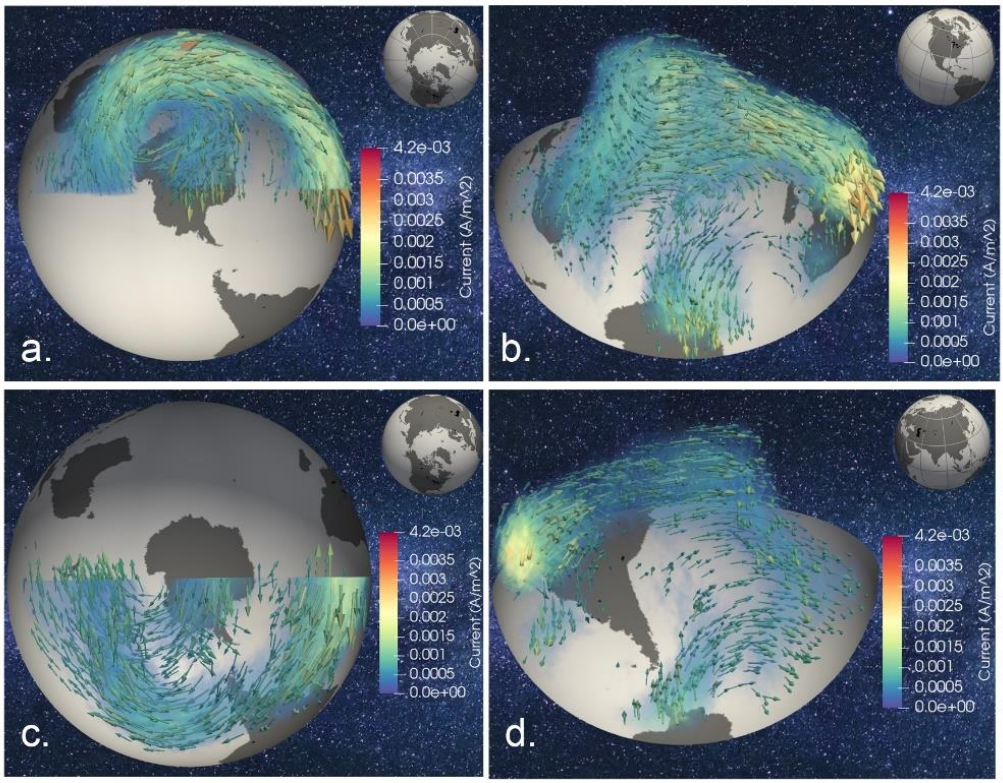

Figure 4: 3-D Structure of the Recovered Core Current Model.

a. Top View of the Eurasia Hemisphere Current Model: This profile displays the 0-180° meridian at the North Pole. Gray sphere sections represent the CMB surface of the Southern Hemisphere (inner surface of the sphere), with an overlay map indicating specific positions. b. Side View of the Current Model depicted in Fig. 4a. The dynamics and spatial arrangement of the currents are further detailed in Movie S2, the animated version of this figure. c. Top View of the Current Model in the American Hemisphere: This profile shows the 180°-360° meridian at the North Pole. Gray sphere sections again mark the CMB surface of the Southern Hemisphere (inner surface of the sphere). d. Side View of the Current Model depicted in Fig. 4c. For an animated and dynamic representation of this model, refer to Movie S3.

The most intense currents in both hemispheres are identified as the equatorial gyre currents near the CMB, consistent with the *x*-direction model sections shown in Figs. 2a and 3a. In the deeper core, a mid-scale toroidal gyre branches off from the inner side of this intense equatorial gyre, as depicted in Fig. 4a. This mid-scale gyre primarily originates from the Eurasia hemisphere, extending down to the core's center. From the side view in Fig. 4b, it's evident that this inner gyre also extends vertically, spanning from the Northern Hemisphere's high-latitude regions to the South Pole's high latitudes.

The other part of the mid-scale toroidal gyre is illustrated in the sections for the other hemisphere (Figs. 4c and 4d). As an integral part of the inner gyre circulation, these flows continue in a clockwise direction, merging into the outer, more intense equatorial gyre (Fig. 4c). From the side view in this hemisphere, depicted in Fig. 4d, the inner gyre currents extend to the high-latitude region below the Antarctic continent, connecting with the middle-scale shallow gyre in the region (Fig. 3e). In summary, alongside the prominent large-scale equatorial gyre, there appears to be a tangentially oriented, cylindrical mid-scale toroidal gyre deep within the core, contributing to a complex overall circulation pattern.

To evaluate the inverted equivalent magnetization source, we estimated the radial magnetic flux at the CMB based on this source, as shown in Fig. 5. The uncertainty of this map is approximately 0 to 6.62 A/m, inferred from the inverse error level of 1%.

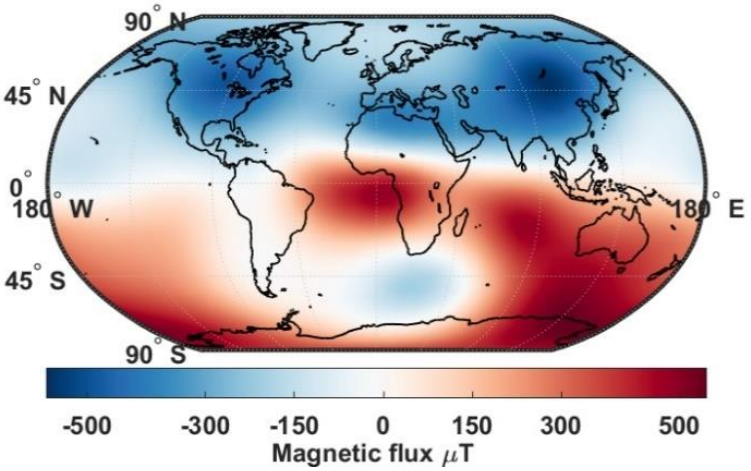

Figure 5: Radial Magnetic Flux on the CMB Estimated Using the Swarm Dataset. The continent shapes provide orientation.

4. Discussion

Although our proposed method aims to invert an equivalent magnetization with accurate location and distribution to improve data modeling accuracy, and the details of current circulation are thoroughly analyzed in the experimental section, it is important to clarify that the primary objective of this study is not to invert the currents in the core. This is because volume magnetization sources, such as those shown in Fig. 1f, are often complex and challenging to interpret. Therefore, it is necessary to transform these into more comprehensible forms, like the current circulation model, which offers an enhanced perspective compared to the conventional ambient magnetization volume, thereby facilitating the interpretation of geomagnetic field data.

Estimating the depth of the current source within the Earth's core inherently involves biases, as evidenced by our synthetic experiment. Although the equivalent magnetization source was accurately placed in terms of depth, the resultant current source showed a depth bias, being approximately 600 km shallower. This bias may arise from three key factors: Firstly, observational data inherently contain limited information, often missing crucial aspects of the

384 actual magnetization vector source, particularly where opposing magnetization is negated by the
385 dominant dipole field. Secondly, the inversion process for a magnetization source is
386 characteristically non-unique, making the derived current source an approximated, and
387 potentially divergent, representation of the actual source. Thirdly, our inverse method is not
388 tailored for precise 3-D current modeling; it is designed to provide an auxiliary, equivalent
389 source model to enhance understanding of the geomagnetic field, rather than to replicate the
390 actual source depth accurately. These factors collectively underscore the challenges in accurately
391 determining the depth of current sources in geomagnetic field modeling. Analogous to findings
392 from our synthetic experiment, it is plausible that the depths of current sources in the IGRF and
393 Swarm examples are shallower than the actual sources. This suggests that the true depth of the
394 actual source model might be approximately 600 km deeper than our estimates. Therefore, this
395 depth bias, or inherent uncertainty, must be carefully considered and accounted for in the
396 interpretation of any dataset.

397 To assess the similarity in distribution between the estimated models and the actual fluid
398 dynamics within the core's interior, we reference results from previous dynamo research.
399 Initially, we compare the radial magnetic flux derived in our study with findings from dynamo
400 area studies. Jackson (2003) analyzed MAGSAT satellite data, identifying intense flux spots or
401 bands in the equatorial regions on the CMB, and presented a radial flux map with flux intensity
402 ranging approximately between [-900 μT , 900 μT]. Korte & Holme (2010) constructed the
403 time-averaged field structure at the CMB over four different time scales. When comparing our
404 results (as illustrated in Fig. 5) with the corresponding radial field maps from these studies—
405 specifically the 2000 BC map in Jackson (2003) and the average field for 1840 AD to 1950 AD
406 in Korte & Holme (2010)—a similarity in the distribution of fields can be observed. All maps

exhibit intense flux patches primarily in the equatorial and polar regions. The numerical range of our map, [-500 μT , 500 μT] (Fig. 5a), aligns more closely with the results of Korte & Holme (2010) ([-400 μT , 400 μT]) than with those of Jackson (2003). Furthermore, Jackson (2003) hypothesized that these intense flux spots might be associated with equatorial fluid structures near the CMB. Our current model supports this hypothesis, as shown in Figs. 2d and 3d, where an intense equatorial current is observed beneath the region, dominating the circulation pattern.

Secondly, Stump and Pollack (1998) estimated a 2-D spherical current sheet model of the Earth's inner core by inverting spherical harmonic coefficients, based on Maxwell's equations. Their analysis resulted in a 2-D map depicting current flow directions, forming a complete global circulation pattern. The surface circulation pattern they presented shows remarkable similarity to our 3-D current circulation model on the CMB surface, as depicted in Figs. 2d-f and 3d-f. Both models feature a dominant equatorial gyre linked to a retrograde current beneath the South Atlantic Ocean, two weaker current gyres beneath Siberia and Canada, and a singular gyre in the Antarctic region. Moreover, the direction and intensity trends of these current flows are strikingly consistent across both models.

Although the current models derived from the IGRF and Swarm datasets display remarkable similarities in their circulation patterns, there are notable differences between them. We attribute these discrepancies to two primary factors. First, the IGRF-13's maximum spherical harmonic degree expansion is 13. While this represents a significant improvement in capturing smaller-scale internal signals compared to previous versions, the direct measurements of the geomagnetic field by the Swarm satellites encompass a broader range of scale signals and inferences. This, we believe, is the principal factor contributing to the observed differences between the models. Second, the datasets differ in their collection timeframes. The IGRF dataset

was compiled with a 'frozen' time parameter set to January 1, 2023, whereas the Swarm dataset consists of data filtered from measurements taken during August 22-27, 2022, between 22:00 and 03:00 local time. From this perspective, it is reasonable to expect some variation in models derived from the same inversion method when the observational datasets differ in such respects.

The dynamo theory posits that both toroidal and poloidal currents coexist within the core. However, it is the toroidal current that contributes to the external magnetic field, while the toroidal field generated by the poloidal current is zero at CMB. So the actual current 3-D pattern in the core cannot be completely recovered due to the limitations of external and long-distance observation data. This study focuses on inverting the magnetic satellite-observed external field and developing equivalent magnetization and current sources to modelling and gain a comprehensive understanding of the geomagnetic field. Nevertheless, it is essential to clarify that exploring the actual current flow patterns and conducting dynamo simulation research are outside the scope of this study. Our forthcoming research will be concentrated on interpreting the secular variations in conjunction with a time serial dataset inverted.

References

Alken, P. et al. International geomagnetic reference field: the thirteenth generation [Dataset]. Earth Planets Space 73, 49 (2021). Retrieved from: https://www.ngdc.noaa.gov/IAGA/vmod/coeffs/igrf13coeffs.txt.

Ayachit, Utkarsh, The ParaView Guide: A Parallel Visualization Application, Kitware, [Software] 2015, ISBN 9781930934306. Retrieved from: https://www.paraview.org/download/.

Buffett, B. (2015), Dipole fluctuations and the duration of geomagnetic polarity

transitions, Geophys. Res. Lett., 42, 7444–7451, doi:10.1002/2015GL065700.

Bloxham, J. & Gubbins, D. The secular variation of earth's magnetic field. Nature 317, 777-781 (1985).

Connerney, J. E. P., Kotsiaros, S., Oliversen, R. J., Espley, J. R., Joergensen, J. L., Joergensen, P. S., et al. (2018). A new model of Jupiter's magnetic field from Juno's first nine orbits. Geophysical Research Letters, 45, 2590-2596. https://doi.org/10.1002/2018GL077312

Davies, C. & Constable, C. Geomagnetic spikes on the core-mantle boundary. *Nat. Commun.* **8**, 15593 (2017).

Demina, I. M., & Farafonova, Y G. (2016). Inverse problem for the current loop model: Possibilities and restrictions. Geomagnetism and Aeronomy, 56, 415–425. https://doi.org/10.1134/s0016793216030038

Dampney, C. N. G., 1969, The equivalent source technique: Geophysics, 34, 39–53, doi: 10.1190/1.1439996.

Geuzaine C. and J.-F. Remacle. Gmsh: a three-dimensional finite element mesh generator with built-in pre- and post-processing facilities [Software]. International Journal for Numerical Methods in Engineering 79(11), pp. 1309-1331, 2009. Retrieved from: : https://gmsh.info/#Download.

Hansen R. O., and Y. Miyazaki, 1984, Continuation of potential fields between arbitrary surfaces: Geophysics, 49, 787–795, doi: 10.1190/1.1441707.

Hood, L. L., Torres, C. B., Oliveira, J. S., Wieczorek, M. A., & Stewart, S. T. (2021). A new large-scale map of the lunar crustal magnetic field and its interpretation. *Journal of*

Geophysical Research: Planets, 126, e2020JE006667. https://doi.org/10.1029/2020JE006667

Hulot, G., Eymin, C., Langlais, B., Mandea, M. & Olsen, N. Small-scale structure of the geodynamo inferred from Oersted and Magsat satellite data. Nature 416, 620-623 (2002).

Jackson, A. Intense equatorial flux spots on the surface of the earth's core. Nature 424, 760-763 (2003).

Monika Korte, Richard Holme, On the persistence of geomagnetic flux lobes in global Holocene field models, Physics of the Earth and Planetary Interiors, 182(3–4), 2010, 179-186, https://doi.org/10.1016/j.pepi.2010.08.006.

Kother L, Magnus D. Hammer, Christopher C. Finlay, Nils Olsen, An equivalent source method for modelling the global lithospheric magnetic field, *Geophysical Journal International*, Volume 203, Issue 1, October 2015, Pages 553–566, https://doi.org/10.1093/gji/ggv317

Langlais, B., Thébault, E., Houliez, A., Purucker, M. E., & Lillis, R. J. (2019). A new model of the crustal magnetic field of Mars using MGS and MAVEN. *Journal of Geophysical Research: Planets*, 124, 1542–1569. https://doi.org/10.1029/2018JE005854

Li, Y., M. Nabighian, and D. W. Oldenburg, 2014, Using an equivalent source with positivity for low-latitude reduction to the pole without striation, Geophysics, 79, J81–J90.

Li, Y., and D. W. Oldenburg, 2010, Rapid construction of equivalent sources using wavelets: Geophysics, 75, no. 3, L51–L59, doi: 10.1190/1.3378764.

Li D., Q. Liang, J. Du, S. Sun, Y. Zhang, C. Chen, 2019, Transforming total-field magnetic anomalies into three components using dual-layer equivalent sources, Geophysical Research Letter,47(3), e2019GL084607.

Langlais, B., M. E. Purucker, and M. Mandea (2004), Crustal magnetic field of Mars, *J. Geophys. Res.*, 109, E02008, doi:10.1029/2003JE002048.

Mayhew, M. A. (1979), Inversion of satellite magnetic anomaly data, *J. Geophys.*, **45**, 119–128.

Oliveira, J. S., B. Langlais, M. A. Pais, and H. Amit (2015), A modified Equivalent Source Dipole method to model partially distributed magnetic field measurements, with application to Mercury, *J. Geophys. Res. Planets*, 120, 1075–1094. doi:10.1002/2014JE004734.

Olsen N, Friis-christensen E, Floberghagen R et al (2013) The Swarm Satellite Constellation Application and Research Facility (SCARF) and Swarm data products [Dataset]. Earth Planets Space, 65:1189–1200. doi:10.5047/eps.2013.07.001. Retrieved from: https://earth.esa.int/web/guest/swarm/data-access

Peddie, N. W. (1979). Current loop models of the Earth's magnetic field. Journal of Geophysical Research, 84(B9), 4517–4523. https://doi. org/10.1029/JB084iB09p04517.

Purucker, M. E., Ravat, D., Frey, H., Voorhies, C., Sabaka, T., & Acuña, M. H. (2000). An altitude-normalized magnetic map of Mars and its interpretation. Geophysical Research Letters, 27, 2449–2452. https://doi.org/10.1029/2000GL000072

Rong, Z. J., Wei, Y., Klinger, L., Yamauchi, M., Xu, W. Y., Kong, D. L., et al. (2021). A new technique to diagnose the geomagnetic field based on a single circular current loop model. Journal of Geophysical Research: Solid Earth, 126, e2021JB022778. https://doi.org/10.1029/2021JB022778

Starchenko, S.V., Smirnov, A.Y. Volume Currents of Present-Day Magnetic Dipole in the Earth's Core. Izv., Phys. Solid Earth 57, 474–478 (2021). https://doi.org/10.1134/S106935132104008X.

Stump D.R. and Pollack, G.L., A current sheet model for the Earth's magnetic field, Am. J. Phys, 1998, vol. 66, pp. 802–810.

The MathWorks Inc. (2021). MATLAB version: 9.11.0.1873467 (R2021b) [Software]. The MathWorks Inc. Retrieved from https://www.math-works.com

Whaler, K. A. D. Gubbins, Spherical harmonic analysis of the geomagnetic field: an example of a linear inverse problem, Geophysical Journal International, \65(3), June 1981, Pages 645–693, https://doi.org/10.1111/j.1365-246X.1981.tb04877.x

Zidarov, D. P., T. Petrova, Representation of the earth's magnetic field as a field of a circular loop, C. R. Acad. Bulg. Sci., 27, 203–206, 1974.

Zuo, B., Hu, X., Leão-Santos, M., Wang, L. & Cai, Y. Downward continuation and transformation of total-field magnetic anomalies into magnetic gradient tensors between arbitrary surfaces using multilayer equivalent sources. Geophys. Res. Lett. 47, e2020GL088678 (2020).

Zuo, B. et al. 3-D magnetic unstructured inversion. J. Geophys. Res. Solid Earth 126, e2021JB022668 (2021).

Open Research

The magnetic dataset in Section 3.1 is extracted from the IGRF model (Alken et. al, 2021). The satellite magnetic observations are obtained from the European Space Agency (ESA) (Olsen et al, 2013). MATLAB (The Mathworks, 2021) is employed for plotting the 2-D figures. The unstructured meshes used in this study are generated using Gmsh (Geuzaine & Remacle, 2009). Paraview (Ayachit & Utkarsh, 2015) is utilized for visualizing the 3-D models.

Supplementary Materials

Supplementary Text

Figs. S1 to S3

Dataset S1

Movie S1 to S3

Acknowledgements

Competing interests

The authors have no conflicts of interest to declare.

Additional information